applied sciences

MDPI

Article

Analysis and Implementation of a Hybrid DC Converter with Wide Voltage Variation

Bor-Ren Lin * and Yue-Ying Zhuang

Department of Electrical Engineering, National Yunlin University of Science and Technology, Yunlin 640, Taiwan; m10912004@yuntech.edu.tw

* Correspondence: linbr@yuntech.edu.tw

Abstract: A new hybrid DC converter is proposed and implemented to have wide voltage variation operation and bidirectional power flow capability for photovoltaic power applications. The hybrid DC converter, including a half- or full-bridge resonant circuit, is adopted to realize the bidirectional power operation and low switching losses. To overcome the wide voltage variation problem (60 V–480 V) from photovoltaic panels due to sunlight intensity, the full-bridge structure or half-bridge structure resonant circuit is used in the presented converter to implement high or low voltage gain under a low or high input voltage condition. Using a pulse frequency modulation (PFM) scheme, the voltage transfer function of the resonant circuit is controlled to regulate the load voltage. Due to the symmetric circuit structures used on the primary and the secondary sides in the proposed converter, the bidirectional power flow can be achieved with the same circuit characteristics. Therefore, the proposed converter can be applied to battery stacks to achieve charger and discharger operations. Finally, a 400 W prototype is implemented, and the performance of the proposed hybrid DC converter is confirmed by the experiments.

Keywords: hybrid DC converter; bidirectional power flow; wide voltage variation; soft switching

check for updates

Citation: Lin, B.-R.; Zhuang, Y.-Y. Analysis and Implementation of a Hybrid DC Converter with Wide Voltage Variation. *Appl. Sci.* **2021**, *11*, 10211. https://doi.org/10.3390/app112110211

Academic Editor: Gilsoo Jang

Received: 31 August 2021
Accepted: 29 October 2021
Published: 31 October 2021

Publisher's Note: MDPI stays neutral with regard to jurisdictional claims in published maps and institutional affiliations.

Copyright: © 2021 by the authors. Licensee MDPI, Basel, Switzerland. This article is an open access article distributed under the terms and conditions of the Creative Commons Attribution (CC BY) license (https://creativecommons.org/licenses/by/4.0/).

1. Introduction

Bidirectional DC converters [1–6] have been proposed to interface between the different DC voltage buses for renewable energy sources, battery chargers/dischargers, uninterrupted power supplies, and electric vehicles. For electric vehicle applications [7,8], bidirectional power factor correctors and bidirectional DC converters have been proposed to realize grid-to-vehicle and vehicle-to-grid operations. Phase-shift pulse-width modulation (PWM) converters have been proposed in [9,10] to realize a forward power flow operation with a voltage step-down operation, and achieve reverse power flow with a voltage step-up operation. The main drawbacks of phase-shift PWM converters are a high freewheeling current and hard switching loss at light load conditions. Dual active bridge (DAB) converters have been studied and proposed in [11–14] to realize bidirectional power flow using a phase-shift PWM technique and duty cycle control. However, two control variables, the phase-shift angle and duty cycle, are more difficult to be calculated and derived compared to the other bidirectional DC converters. Symmetric CLLC converters have been proposed in [15,16] to accomplish forward and reverse power flow operations for DC distribution systems and battery charging/discharging systems. The primary-side and secondary-side have the same circuit structures in CLLC converters. Therefore, the forward and backward voltage transfer functions are identical and the circuit characteristics for both power flows are identical. The power switches can be turned on at soft switching operation due to the circuit characteristics of the resonant converter with frequency modulation. The main drawback of the CLLC converter is a narrow voltage operation range due to its low voltage gain. Therefore, the CLLC converter cannot work well under wide voltage variation conditions, such as solar power applications. To realize wide voltage variation capability, cascade DC converters have been proposed in [17,18], with a buck or boost

circuit on the front-stage and a PWM converter on the rear stage. The main problem of cascade DC converters is high conduction loss. PWM converters or resonant converters with serial–parallel circuit structures have been studied in [19–22] to realize wide input voltage operation ($V_{in,max}/V_{in,min} < 4$). However, only forward power flow can be realized in these circuit topologies.

According to the foregoing studies, a DC hybrid symmetric resonant converter for battery charging and discharging is proposed in this paper. One AC switch and one hybrid half/full-bridge circuit structure are used on both the primary-side and secondary-side to achieve wide voltage input operation and bidirectional power flow operation. The benefits of the proposed converter are as follows: (1) wide voltage operation from 60 V–480 V input; (2) symmetric circuit on both the primary and secondary sides to have the same voltage transfer function for backward and reverse power operations; and (3) soft switching operation on power semiconductors due to resonant circuit characteristics with frequency modulation. The proposed converter can be applied to photovoltaic power applications or battery charging/discharging systems. A 400 W prototype is provided to verify the proposed bidirectional power flow converter. The experimental results demonstrated that the maximum circuit efficiency of the prototype is approximately 93.6%. The circuit diagram of the proposed hybrid DC converter is discussed in Section 2. In Section 3, the principle operations of the converter are provided. The circuit characteristics and a design example are described in Section 4. Experimental results are provided and discussed in Section 5, to verify the feasibility of the theoretical discussions. The conclusions of the proposed circuit are described in Section 6.

2. Circuit Diagram of the Proposed Hybrid DC Converter

Figure 1a gives the circuit diagram of a hybrid DC converter. The primary and secondary sides of the isolated transformer have the same circuit structure. Full-power switches and one AC switch are used on each side. The AC switches S_{ac1} and S_{ac2} are implemented by two switches connected back-to-back. On each side, the resonant circuit can be operated at the full-bridge structure (S_1–S_4) or half-bridge structure (S_1, S_2, and S_{ac1}), related to low or high input voltage range conditions. For forward power flow operation, S_5–S_8 are all inactive. Therefore, the right-hand side circuit operates as a half-wave (S_{ac2} is on) or full-wave (S_{ac2} is off) diode rectifier. The proposed hybrid converter has three operation modes to achieve wide input voltage variation. In each operation mode, the circuit can achieve two times the input voltage range. Therefore, the wide input voltage range variation $V_{in,max} = 8V_{in,min}$ (where $V_{in,min}$ = 60 V and $V_{in,max}$ = 480 V) can be implemented in the proposed converter. When $V_{in,min} \leq V_{in} < 2V_{in,min}$, the high voltage gain is needed in the proposed converter. Therefore, the full-bridge resonant circuit (S_{ac1} is off) is operated on the left-hand side and the half-wave diode rectifier (or voltage doubler rectifier) (S_{ac2} is on) is operated on the right-hand side, as shown in Figure 1b, to achieve the maximum voltage gain. When $2V_{in,min} \leq V_{in} < 4V_{in,min}$, the half-bridge resonant circuit (S_{ac1} is on and S_3 and S_4 are off) is used on the left-hand side and half-wave diode rectifier (S_{ac2} is on) is selected on the right-hand side (Figure 1c) to obtain medium voltage gain. If $4V_{in,min} \leq V_{in} < 8V_{in,min}$, the half-bridge resonant circuit (S_{ac1} is on and S_3 and S_4 are off) and full-wave diode rectifier (S_{ac2} is off) are selected on the left-hand side and right-hand side, respectively (Figure 1d), to obtain the minimum voltage gain. For backward power flow operation (Figure 1e), S_1–S_4 are off and S_{ac1} is on. Thus, the left-hand side circuit operates as a half-wave diode rectifier. S_5–S_8 are controlled with the PFM scheme to deliver power from the V_o terminal to the V_{in} terminal.

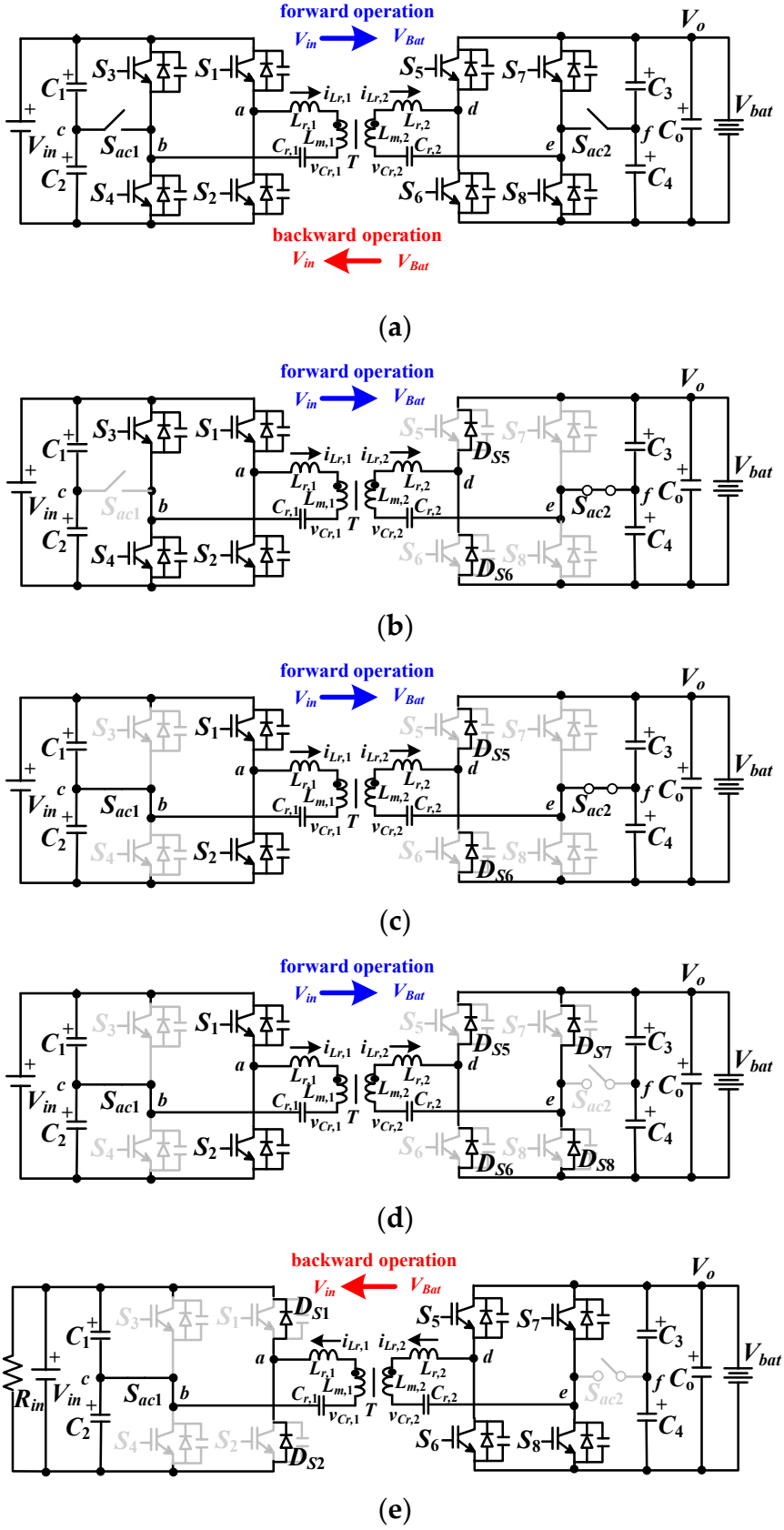


Figure 1. Presented hybrid DC converter: (**a**) circuit structure; (**b**) low voltage range input under forward power flow; (**c**) medium voltage range input under forward power flow; (**d**) high voltage range input under forward power flow; (**e**) under baclward power flow operation.

3. Operation Principle

Two main advantages of the proposed converter are wide voltage variation operation and bidirectional power flow operation. Under forward power flow operation, three operations modes, shown in Figure 1b–d, can be operated according to the low, medium and high voltage range inputs. Under backward power flow operation (Figure 1e), power switches on the secondary side are controlled to reverse the power flow from the load side to the input side.

3.1. Low Voltage Range Input ($V_{in,min} \leq V_{in} < 2V_{in,min}$) under Forward Power Flow

If the input voltage is in the low voltage range, the full-bridge resonant circuit is used on the primary side and the half-wave diode rectifier is adopted on the secondary side to achieve the maximum voltage gain. Therefore, S_{ac1} and S_5–S_8 are off and S_{ac2} is on, as shown in Figure 1b. From the pulse-width modulation signals of S_1–S_4, D_{S5}, and D_{S6}, one can observe that there are eight switching states (Figure 2a) in every switching cycle if f_{sw} (switching frequency) $< f_r$ (resonant frequency). The circuit components are assumed as $C_{r,2} = n^2 C_{r,1}$ and $L_{r,2} = L_{r,1}/n^2$, where $n = n_p/n_s$, to simplify the circuit analysis. Therefore, the series resonant frequency on the primary and secondary sides are identical, $f_{r,1} = 1/(2\pi\sqrt{L_{r,1}C_{r,1}}) = f_{r,2} = 1/(2\pi\sqrt{L_{r,2}C_{r,2}})$. The state circuit operations related to the eight switching states are provided in Figure 2b–i.

State 1 [$t_0 \leq t < t_1$]: When $t = t_0$, $v_{S1,ce} = v_{S4,ce} = 0$. $i_{Lr,1}(t_0) < 0$ will flow through diodes D_{S1} and D_{S4}. Then, S_1 and S_4 can turn on at zero-voltage switching. The secondary side current $i_{Lr,2}$ flows through diode D_{S5} to charge capacitor C_3. In this state, $i_{Lr,1}$ increases from a negative value to zero ampere.

State 2 [$t_1 \leq t < t_2$]: When $t > t_1$, $i_{Lr,1}$ becomes a positive value. Then $i_{Lr,1}$ flows through S_1 and S_4. Forward power flow is from V_{in} to V_o in State 2 operation. The converter leg voltages are $V_{ab} = V_{in}$ and $V_{de} = V_{C3} = V_o/2$. The resonant frequency in State 2 is given as $f_{r,1} = 1/(2\pi\sqrt{L_{r,1}C_{r,1}})$.

State 3 [$t_2 \leq t < t_3$]: When f_{sw} is less than $f_{r,1}$, $i_{Lr,2}$ will be decreased to zero at time t_2. The rectifier diode D_{S5} becomes off. In State 3, the resonant frequency of $i_{Lr,1}$ is $f_{p,1} = 1/(2\pi\sqrt{C_{r,1}(L_{m,1} + L_{r,1})})$. No power is transferred to output load in this state.

State 4 [$t_3 \leq t < t_4$]: When $t = t_3$, S_1 and S_4 are turned off. $i_{Lr,1}$ discharges C_{S2} and C_{S3} where C_{S2} and C_{S3} are the output capacitors of S_2 and S_3, respectively. If the primary current $i_{Lr,1}(t_3) = \hat{i}_{Lm,1} > V_{in}\sqrt{2C_{S,p}/L_{r,1}}$, where $C_{S,p} = C_{S1} = C_{S2} = C_{S3} = C_{S4}$ (C_{S1}–C_{S3} are output capacitors of S_1–S_4, respectively) and $\hat{i}_{Lm,1}$ is the peak value of $i_{Lm,1}$, then C_{S2} and C_{S3} can be discharged to zero voltage at time t_4.

State 5 [$t_4 \leq t < t_5$]: The capacitor voltages $v_{CS2} = v_{CS3} = 0$ (or $v_{S2,ce} = v_{S3,ce} = 0$) at time t_4. Then $i_{Lr,1}(t_4) > 0$ will flow through D_{S2} and D_{S3}. The zero-voltage turn-on operation of S_2 and S_3 can be implemented after time t_4. The secondary side current $i_{Lr,2}$ will be decreased and D_{S6} becomes forward biased. The primary curent $i_{Lr,1}$ is decreased and capacitor C_4 is charged in State 5.

State 6 [$t_5 \leq t < t_6$]: After $t > t_5$, $i_{Lr,1} < 0$. Then, D_{S2} and D_{S3} become reverse biased. $i_{Lr,1}$ will flow through S_2 and S_3. In State 6, $i_{Lr,1}$ is decreased and C_4 is charged by $i_{Lr,2}$. The resonant frequency is $f_{r,1} = 1/(2\pi\sqrt{L_{r,1}C_{r,1}})$.

State 7 [$t_6 \leq t < t_7$]: At $t = t_6$, the secondary side current $i_{Lr,2} = 0$ and D_{S6} becomes reverse biased. The resonant frequency in this state is $f_{p,1} = 1/(2\pi\sqrt{C_{r,1}(L_{m,1} + L_{r,1})})$.

State 8 [$t_7 \leq t < T_{sw} + t_0$]: When $t = t_7$, S_2 and S_3 turn off. $i_{Lr,1}(t_7) < 0$ will discharge C_{S1} and C_{S4}. The one switching period ends at time $T_{sw} + t_0$.

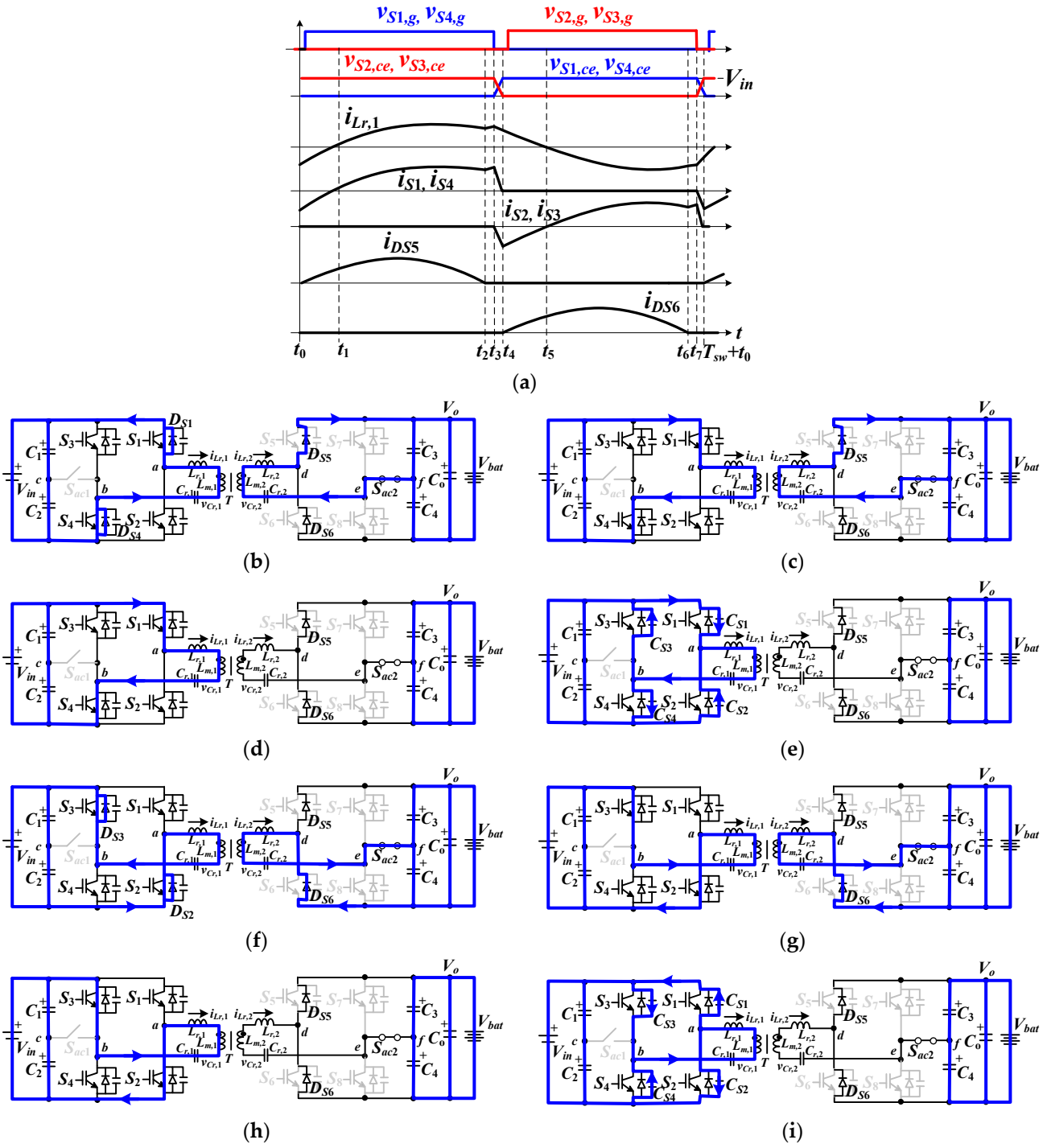


Figure 2. PWM signals and state circuits under low voltage range input and forward power flow: (**a**) PWM signals; (**b**) State 1; (**c**) State 2; (**d**) State 3; (**e**) State 4; (**f**) State 5; (**g**) State 6; (**h**) State 7; (**i**) State 8.

3.2. Medium Voltage Range Input ($2V_{in,min} \leq V_{in} < 4V_{in,min}$) under Forward Power Flow

When a medium voltage range is input to the proposed converter, the half-bridge resonant circuit is operated on the left-hand side (Figure 1c). Since the input voltage of the resonant circuit is $\pm V_{in}/2$ instead of $\pm V_{in}$ in Figure 1b, the voltage gain in Figure 1c is only 1/2 of the voltage gain in Figure 1b. One can observe in Figure 1c that S_{ac1} is on and S_3 and S_4 are off. Only S_1 and S_2 are operated with the PFM scheme. S_{ac2} is on and the half-wave diode rectifier or voltage doubler rectifier is operated on the secondary side. Since the half-bridge resonant circuit (Figure 1c) and full-bridge resonant circuit (Figure 1b) have

similar operation states, the circuit operations of the proposed converter under a medium voltage range input are neglected in this subsection.

3.3. High Voltage Range Input ($4V_{in,min} \leq V_{in} < 8V_{in,min}$) under Forward Power Flow

When the input voltage is in the high voltage range, the half-bridge resonant circuit is operated on the left-hand side and the full-wave diode rectifier (S_{ac2} is off) is operated on the right-hand side, as shown in Figure 1d. Comparing Figure 1c,d, the leg voltage v_{de} is $\pm V_o$ in Figure 1d instead of $\pm V_o/2$ in Figure 1c with voltage doubler rectifier structure. Therefore, the converter in the Figure 1d operation has less voltage gain than the Figure 1c operation. From Figure 1b–d, it can be concluded that the Figure 1b circuit is selected to control the load voltage with the maximum voltage gain under a low voltage range input condition, and the Figure 1d circuit is selected to regulate the load voltage with the minimum voltage gain under high voltage range input conditions. The circuit operation in Figure 1d is similar to the circuit operation in Figure 1b,c. Thus, the operation principle of the Figure 1d circuit is neglected in this subsection.

3.4. Backward Power Flow

If the converter is operated at backward power operation, the power flow is transferred from V_o to V_{in}, as shown in Figure 1e. Since V_{in} is controlled at 400 V, the half-wave diode rectifier is used on the left-hand side. Therefore, S_{ac1} is on. The full-bridge resonant circuit is operated on the right-hand side so that S_{ac2} is off and S_5–S_8 are operated with the PFM scheme. Figure 3a provides the switching signals of the converter under backward power flow in every switching cycle. Figure 3b–i show these state equivalent circuits.

State 1 [$t_0 \leq t < t_1$]: C_{S5} and C_{S8} are discharged to zero voltage at t_0. $i_{Lr,2}(t_0)$ is negative so that D_{S5} anf D_{S8} are forward biased. Active switches S_5 and S_8 can be turned on after t_0 to have soft switching turn-on operation. Since $i_{Lr,1} > 0$, D_{S1} is forward biased and C_1 is charged.

State 2 [$t_1 \leq t < t_2$]: At t_1, $i_{Lr,2} > 0$. Thus, i_{Lr2} flows through S_5 and S_8. Backward power is transferred from V_o to V_{in} in this state. One can obtain $V_{ab} = V_{C1} = V_{in}/2$ and $V_{de} = V_o$. The resonant frequency is $f_{r,2} = 1/(2\pi\sqrt{L_{r,2}C_{r,2}}) = 1/(2\pi\sqrt{L_{r,1}C_{r,1}}) = f_{r,1}$.

State 3 [$t_2 \leq t < t_3$]: If $f_{sw} < f_{r,1}$, $i_{Lr,1} = 0$ at t_2 and D_{S1} is reverse biased. The resonant frequency on right-hand side circuit is $f_{p,2} = 1/(2\pi\sqrt{C_{r,2}(L_{m,2} + L_{r,2})})$ and $f_{p,2} < f_{p,1}$.

State 4 [$t_3 \leq t < t_4$]: S_5 and S_8 are off at t_3. Due to $i_{Lr,2}(t_3) > 0$, C_{S6} and C_{S7} are discharged by $i_{Lr,2}$.

State 5 [$t_4 \leq t < t_5$]: C_{S6} and C_{S7} are discharged to zero voltage at t_4. Since $i_{Lr,2}(t_4) > 0$, $i_{Lr,2}$ flows through D_{S6} anf D_{S7}. Then, S_6 and S_7 turn on after t_4 to achieve soft switching turn-on operation. Owing to $i_{Lr,1} < 0$, D_{S2} becomes forward biased and C_2 is charged.

State 6 [$t_5 \leq t < t_6$]: After t_5, $i_{Lr,2} < 0$ and $i_{Lr,2}$ flows through S_6 and S_7. Backward power flow is from V_o to V_{in} in this state operation.

State 7 [$t_6 \leq t < t_7$]: $i_{Lr,1} = 0$ at t_6. Then, D_{S2} is off. The resonant frequency on the right-hand side circuit is $f_{p,2} = 1/(2\pi\sqrt{C_{r,2}(L_{m,2} + L_{r,2})})$.

State 8 [$t_7 \leq t < T_{sw} + t_0$]: S_6 and S_7 turn off at t_7. Since $i_{Lr,2}(t_7) < 0$, $i_{Lr,2}$ discharges C_{S5} and C_{S8}. At time $T_{sw} + t_0$, C_{S5} and C_{S8} are discharged to zero voltage.

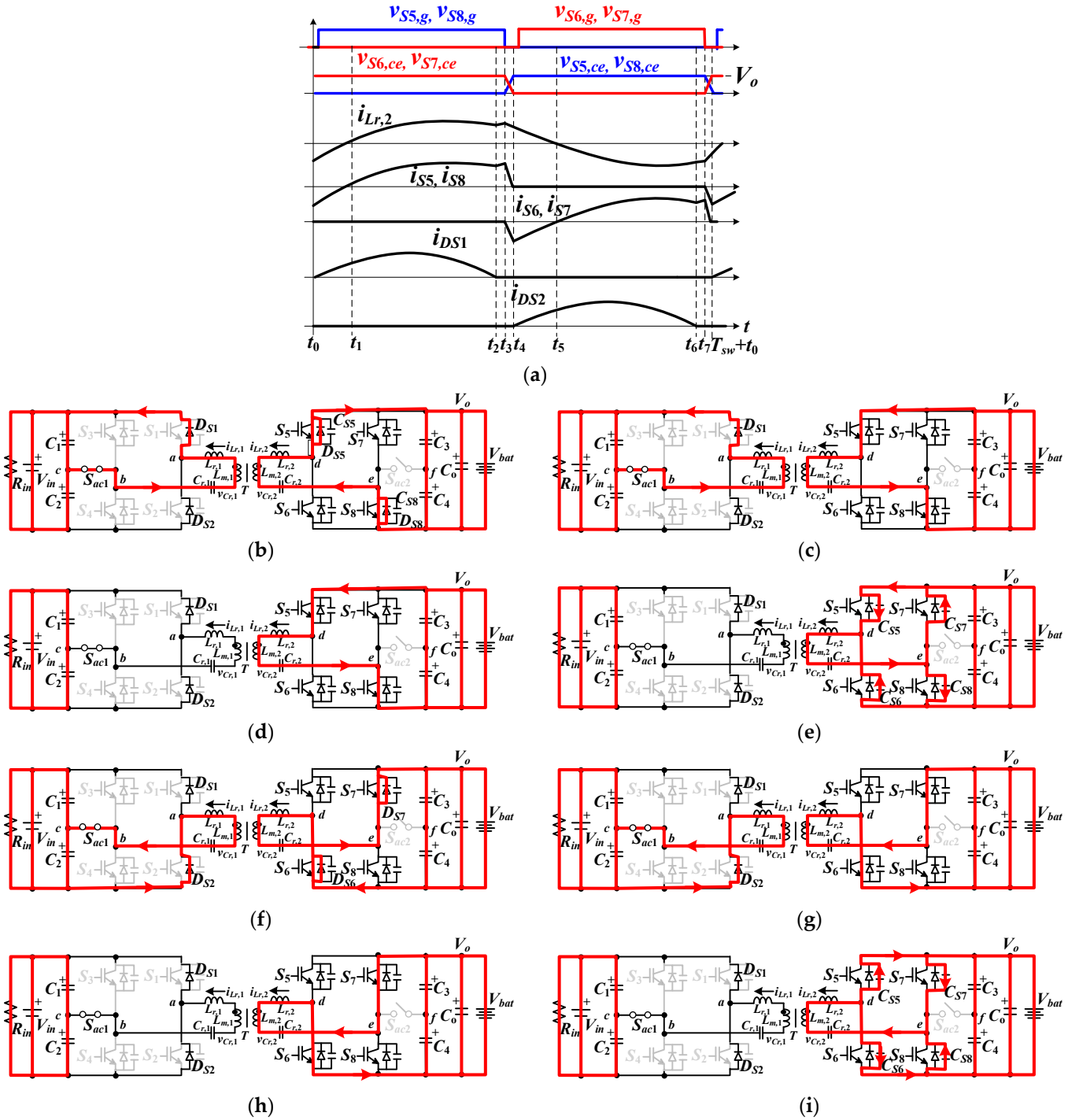


Figure 3. PWM signals and state circuits under backward power flow: (**a**) PWM signals; (**b**) State 1; (**c**) State 2; (**d**) State 3; (**e**) State 4; (**f**) State 5; (**g**) State 6; (**h**) State 7; (**i**) State 8.

4. Circuit Characteristics and Design Example

There are four operating modes in the proposed circuit, as shown in Figure 1. In each mode, the PFM scheme is selected to control the active switches so that the voltage gain of the resonant circuit is depended on the switching frequency. The equivalent resonant circuits in Figure 1b–e can be redrawn and is shown in Figure 4. For the forward power flow operation, the leg voltage V_{ab} is a square-wave voltage with $\pm V_{in}$ (low voltage range input condition) or $\pm V_{in}/2$ (medium and high voltage range input conditions). The leg voltage V_{de} on the right-hand side of the converter is a square-wave voltage with $\pm V_o/2$ (low

and medium voltage range input conditions) or $\pm V_o$ (high voltage range input condition). For the backward power flow operation, the leg voltages $V_{ab} = \pm V_{in}/2$ and $V_{de} = \pm V_o$. According to the Fourier Series Analysis, the square-wave voltage can be expressed as the summation of the fundamental sinewave voltage and the higher-order harmonic components. Since the higher-order harmonic components are less than the fundamental frequency voltage, only the fundamental sinewave voltage is adopted in the following consideration. The analysis of fundamental frequency is used in [23] to analyze the resonant converter and simplify the circuit analysis. Figure 5 provides the resonant circuits with the fundamental frequency analysis method under four operating modes. If the leg voltage $V_{ab} = \pm V_{in}/2$ (Figure 4b–d) or $\pm V_{in}$ (Figure 4a), then its fundamental root-mean-square (*rms*) voltage can be obtained as $V_{ac,f} = \sqrt{2}V_{in}/\pi$ (Figure 5b–d) or $2\sqrt{2}V_{in}/\pi$ (Figure 5a). Similarly, the rms voltage $V_{de,f} = \sqrt{2}V_o/\pi$ (Figure 5a,b) or $2\sqrt{2}V_o/\pi$ (Figure 5c,d) if $V_{de} = \pm V_o/2$ (Figure 4a,b) or $\pm V_o$ (Figure 4c,d). In Figure 5, $R_{o,e,h}$ and $R_{o,e,f}$ are the fundamental load resistances under the half-wave diode rectifier (Figure 5a,b) and full-wave diode rectifier (Figure 5c) operation with forward power flow operation.

$$R_{o,e,h} = \frac{2n^2}{\pi^2} R_o. \tag{1}$$

$$R_{o,e,f} = \frac{8n^2}{\pi^2} R_o. \tag{2}$$

Similarly, the fundamental load resistance $R_{in,e,h}$ (Figure 5d) under backward power flow operation is given in Equation (3).

$$R_{in,e,h} = \frac{2}{\pi^2 n^2} R_{in}. \tag{3}$$

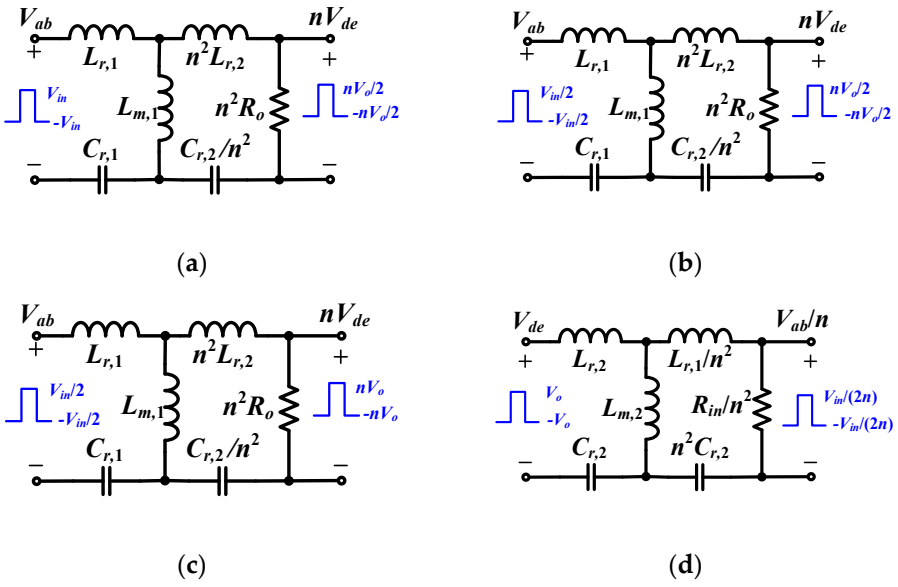


Figure 4. Equivalent resonant circuits under four operating modes: (**a**) low voltage range input with forward power flow; (**b**) medium voltage range input with forward power flow; (**c**) high voltage range input with forward power flow; (**d**) backward power flow operation.

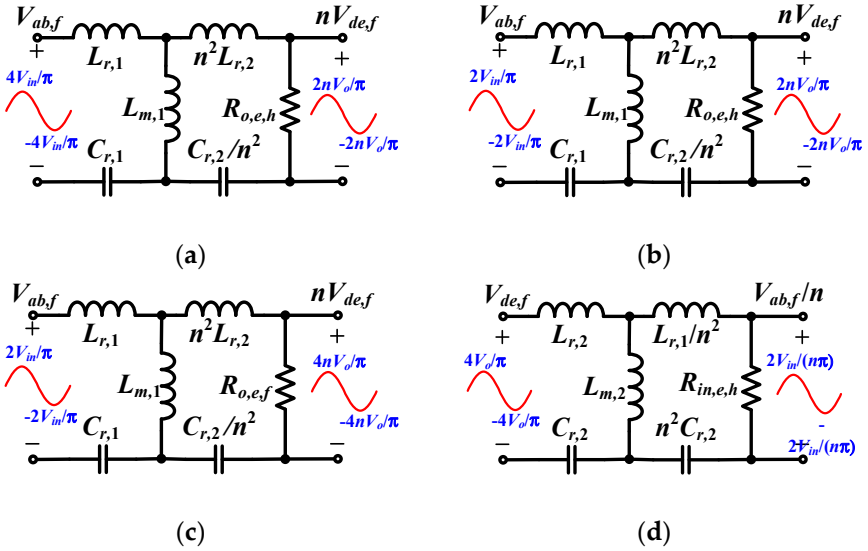


Figure 5. Resonant circuits using fundamental frequency analysis: (**a**) low voltage range input with forward power flow; (**b**) medium voltage range input with forward power flow; (**c**) high voltage range input with forward power flow; (**d**) backward power flow operation.

The voltage transfer functions in Figure 5a–d are derived in Equations (4)–(7), where $M_{ac,F,L}$, $M_{ac,F,M}$, and $M_{ac,F,H}$ are the voltage transfer functions at the low, medium, and high voltage range inputs under forward power flow operation and $M_{ac,B}$ is the voltage transfer function under backward power flow operation.

$$\begin{aligned} M_{ac,F,L}(s) &= \frac{nV_{de,f}}{V_{ac,f}} = \frac{\sqrt{2}nV_o/\pi}{2\sqrt{2}V_{in}/\pi} = \frac{nV_o}{2V_{in}} \\ &= \frac{sL_{m,1}//\left(sn^2L_{r,2}+\frac{n^2}{sC_{r,2}}+R_{o,e,h}\right)}{sL_{r,1}+\frac{1}{sC_{r,1}}+\left[sL_{m,1}//\left(sn^2L_{r,2}+\frac{n^2}{sC_{r,2}}+R_{o,e,h}\right)\right]} \times \frac{R_{o,e,h}}{sn^2L_{r,2}+\frac{n^2}{sC_{r,2}}+R_{o,e,h}} \end{aligned} \quad (4)$$

$$\begin{aligned} M_{ac,F,M}(s) &= \frac{nV_{de,f}}{V_{ac,f}} = \frac{\sqrt{2}nV_o/\pi}{\sqrt{2}V_{in}/\pi} = \frac{nV_o}{V_{in}} \\ &= \frac{sL_{m,1}//\left(sn^2L_{r,2}+\frac{n^2}{sC_{r,2}}+R_{o,e,h}\right)}{sL_{r,1}+\frac{1}{sC_{r,1}}+\left[sL_{m,1}//\left(sn^2L_{r,2}+\frac{n^2}{sC_{r,2}}+R_{o,e,h}\right)\right]} \times \frac{R_{o,e,h}}{sn^2L_{r,2}+\frac{n^2}{sC_{r,2}}+R_{o,e,h}} \end{aligned} \quad (5)$$

$$\begin{aligned} M_{ac,F,H}(s) &= \frac{nV_{de,f}}{V_{ac,f}} = \frac{2\sqrt{2}nV_o/\pi}{\sqrt{2}V_{in}/\pi} = \frac{2nV_o}{V_{in}} \\ &= \frac{sL_{m,1}//\left(sn^2L_{r,2}+\frac{n^2}{sC_{r,2}}+R_{o,e,f}\right)}{sL_{r,1}+\frac{1}{sC_{r,1}}+\left[sL_{m,1}//\left(sn^2L_{r,2}+\frac{n^2}{sC_{r,2}}+R_{o,e,f}\right)\right]} \times \frac{R_{o,e,f}}{sn^2L_{r,2}+\frac{n^2}{sC_{r,2}}+R_{o,e,f}} \end{aligned} \quad (6)$$

$$\begin{aligned} M_{ac,B}(s) &= \frac{V_{ab,f}/n}{V_{de,f}} = \frac{V_{in}}{2nV_o} \\ &= \frac{sL_{m,2}//\left(sL_{r,1}/n^2+\frac{1}{sn^2C_{r,1}}+R_{in,e,h}\right)}{sL_{r,2}+\frac{1}{sC_{r,2}}+\left[sL_{m,2}//\left(sL_{r,1}/n^2+\frac{1}{sn^2C_{r,1}}+R_{in,e,h}\right)\right]} \times \frac{R_{in,e,h}}{sL_{r,1}/n^2+\frac{1}{sn^2C_{r,1}}+R_{in,e,h}} \end{aligned} \quad (7)$$

The following parameters are defined: $Q_{F,h} = \sqrt{L_{r,1}/C_{r,1}}/R_{o,e,h}$, $Q_{F,f} = \sqrt{L_{r,1}/C_{r,1}}/R_{o,e,f}$, $Q_{B,h} = \sqrt{L_{r,2}/C_{r,2}}/R_{in,e,h}$, $K_F = L_{m,1}/L_{r,1}$, $K_B = L_{m,2}/L_{r,2} = K_F$, $F_F = f_{sw}/f_{r,1}$ and $F_B = f_{sw}/f_{r,2} = F_F$. The voltage gains in the four operation modes in

(4)–(7) can be expressed in (8)–(10) for the low, medium, and high voltage range inputs under forward power flow and in (11) for backward power flow operation.

$$\begin{aligned}\left|M_{ac,F,L}(Q_{F,h},K_F,F_F)\right| &= \frac{nV_o}{2V_{in}}\\ &= \frac{1}{\sqrt{\left[1+\frac{1}{K_F}-\frac{1}{K_FF_F^2}\right]^2+Q_{F,h}^2\left[F_F\left(2+\frac{1}{K_F}\right)-\frac{1}{F_F}\left(2+\frac{2}{K_F}-\frac{1}{K_FF_F^2}\right)\right]^2}}.\end{aligned} \quad (8)$$

$$\begin{aligned}\left|M_{ac,F,M}(Q_{F,h},K_F,F_F)\right| &= \frac{nV_o}{V_{in}}\\ &= \frac{1}{\sqrt{\left[1+\frac{1}{K_F}-\frac{1}{K_FF_F^2}\right]^2+Q_{F,h}^2\left[F_F\left(2+\frac{1}{K_F}\right)-\frac{1}{F_F}\left(2+\frac{2}{K_F}-\frac{1}{K_FF_F^2}\right)\right]^2}}.\end{aligned} \quad (9)$$

$$\begin{aligned}\left|M_{ac,F,H}\left(Q_{F,f},K_F,F_F\right)\right| &= \frac{2nV_o}{V_{in}}\\ &= \frac{1}{\sqrt{\left[1+\frac{1}{K_F}-\frac{1}{K_FF_F^2}\right]^2+Q_{F,f}^2\left[F_F\left(2+\frac{1}{K_F}\right)-\frac{1}{F_F}\left(2+\frac{2}{K_F}-\frac{1}{K_FF_F^2}\right)\right]^2}}.\end{aligned} \quad (10)$$

$$\begin{aligned}\left|M_{ac,B}(Q_B,K_B,F_B)\right| &= \frac{V_{in}}{2nV_o}\\ &= \frac{1}{\sqrt{\left[1+\frac{1}{K_B}-\frac{1}{K_BF_B^2}\right]^2+Q_B^2\left[F_B\left(2+\frac{1}{K_B}\right)-\frac{1}{F_B}\left(2+\frac{2}{K_B}-\frac{1}{K_BF_B^2}\right)\right]^2}}.\end{aligned} \quad (11)$$

It is clear that Equations (8)–(11) have a similar voltage transfer function but different DC voltage gain.

In the following sub-section, a design example of the hybrid DC converter is discussed and presented. For forward power flow, the input and output electric parameters are V_{in} = 60 V–480 V, V_o = 40 V–52 V, $I_{o,max}$ = 7.7 A, and $f_{r,1}$ = 100 kHz. For the backward power flow operation, the electric parameters are V_o = 42 V–48 V, V_{in} = 400 V, $P_{in,max}$ = 400 W, and $f_{r,2}$ = 100 kHz. The constant current/constant voltage is adopted to charge the battery under forward power flow operation. If 60 V $\leq V_{in}$ < 120 V (low voltage range), then the full-bridge resonant circuit is operated on the left-hand side and the half-wave diode rectifier is used on the right-hand side of the converter, as shown in Figure 1b. If 120 V $\leq V_{in}$ < 240 V (medium voltage range), then the half-bridge resonant circuit is operated on the left-hand side and half-wave diode rectifier is used on the right-hand side of the converter, as shown in Figure 1c. If 240 V $\leq V_{in} \leq$ 480 V (high voltage range), then the half-bridge resonant circuit and full-wave diode rectifier are is operated on the left-hand side and right-hand side of the converter, respectively, as shown in Figure 1d. Due to the gains of the four mode operations in (8)–(11) having a similar transfer function, the circuit parameters in the laboratory prototype are obtained from low voltage range input (V_{in} = 60 V–120 V) under forward power flow. In the prototype design, the minimum voltage gain $|M_{ac,F,L}|_{min}$ is set at unity under V_{in} = 120 V and V_o = 40 V. The turn-ratio n of T is obtained from Equation (8) and given in Equation (12).

$$n = \left|M_{ac,F,L}\right|_{min} \times \frac{2V_{in,max}}{V_{o,min}} = 1 \times \frac{2 \times 120}{40} = 6. \quad (12)$$

The transformer T is implemented by magnetic core PC40/EE55 with 22 turns on the primary side and 4 turns on the secondary side. Thus, the actual turn-ratio n = 22/4 = 5.5. The maximum and minimum voltage gains at low voltage range input conditions are given in (13) and (14).

$$\left|G_{ac,F,L}\right|_{max} = \frac{nV_{o,max}}{2V_{in,min}} = \frac{5.5 \times 52}{2 \times 60} \approx 2.38. \quad (13)$$

$$\left|G_{ac,F,L}\right|_{min} = \frac{nV_{o,min}}{2V_{in,max}} = \frac{5.5 \times 40}{2 \times 120} \approx 0.92. \quad (14)$$

The gain curves of the transfer function at the low voltage range input condition under K_F = 5 are plotted in Figure 6. Since the maximum voltage gain at V_{in} = 60 V and V_o = 52 V is 2.38 in (13), the quality factor $Q_{F,h}$ = 0.2 is selected to have a peak voltage gain (= 2.5),

which is greater than $|G_{ac,F,L}|_{max} = 2.38$. Therefore, the switching frequency index F_F is created and obtained under V_{in} = 60 V–120 V and V_o = 40 V–52 V. Then, the equivalent resistance $R_{o,e,h}$ at full load is obtained as

$$R_{o,e,h} = \frac{2n^2}{\pi^2} R_o = \frac{2 \times 5.5^2}{3.14159^2} \times \frac{52}{7.7} \approx 41.4\ \Omega. \quad (15)$$

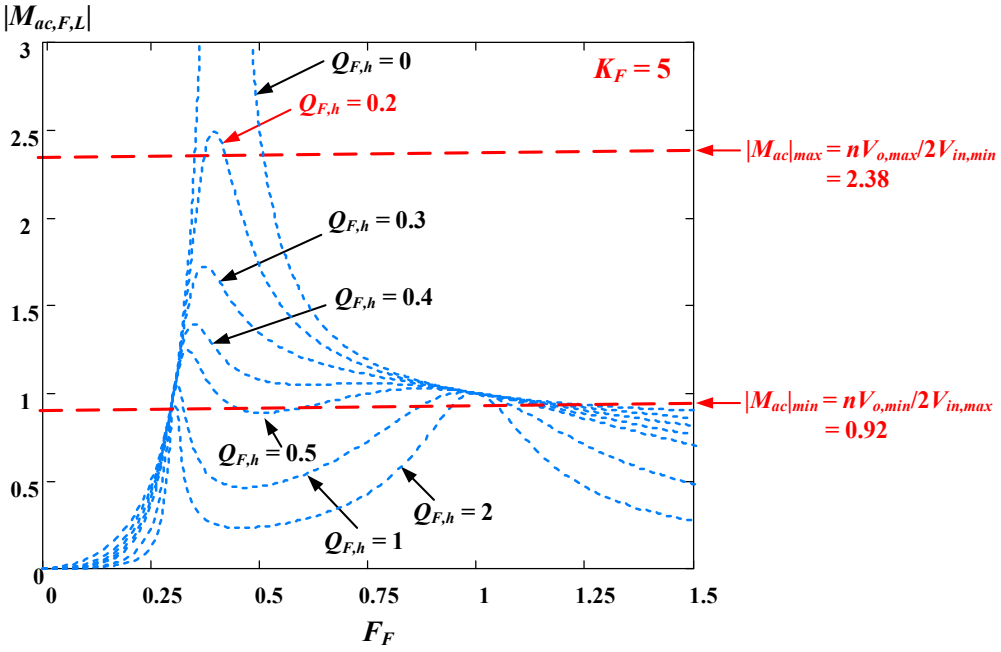


Figure 6. Gain curves of the converter at low voltage range input.

The resonant components on the primary-side of the converter are calculated in Equations (16) and (17).

$$C_{r,1} = 1/(2\pi Q_{F,h} f_{r,1} R_{o,e,h}) \approx 192\ \text{nF}. \quad (16)$$

$$L_{r,1} = Q_{F,h} R_{o,e,h}/(2\pi f_{r,1}) \approx 13\ \mu\text{H}. \quad (17)$$

Since K_F = 5, the magnetizing inductance $L_{m,1} = K_F L_{r,1}$ = 65 µH. The resonant components on the secondary-side of the converter are $L_{r,2} = L_{r,1}/n^2 \approx 0.43$ µH and $C_{r,2} = n^2 C_{r,1} \approx 5.8$ µF. Magnetic cores PC40/EER35 are used to implement $L_{r,1}$ and $L_{r,2}$. S_1–S_4 and S_{ac1} are implemented by power switches FGH60N60 with a 600 V/60 A rating. S_5–S_8 and S_{ac2} are implemented by power switches P80NF12 with a 120 V/80 A rating. The capacitances are $C_1 = C_2$ = 560 µF/400 V, $C_3 = C_4$ = 220 µF/100 V, and C_o = 660 µF/100 V. Table 1 gives the circuit parameters used in the prototype circuit.

Table 1. Circuit parameters used in the prototype circuit.

Items	Parameter
C_1, C_2	560 μF/400 V
C_3, C_4	220 μF/100 V
$C_{r,1}$	192 nF
$C_{r,2}$	5.8 μF
$L_{r,1}$	13 μH
$L_{r,2}$	0.43 μH
$L_{m,1}$	65 μH
S_1–S_4, S_{ac1}	FGH60N60 (600 V/60 A)
S_5–S_8, S_{ac2}	P80NF12 (120 V/80 A)
C_o	660 μH/100 V
Transformer n_p:n_s	22:4

5. Experimental Results

Figure 7 shows the measured input voltage V_{in} and the switch signals S_{ac1} and S_{ac2}. It is clear that S_{ac1} is off and S_{ac2} is on when 60 V $\leq V_{in} <$ 120 V. The converter is operated at a low voltage range input, shown in Figure 1b. If 120 V $\leq V_{in} <$ 240 V, then S_{ac1} and S_{ac2} are both on, and the converter is operated at the medium voltage range input conditions, shown in Figure 1c. If 240 V $\leq V_{in} \leq$ 480 V, then S_{ac1} is on and S_{ac2} is off and the converter is operated at the high voltage range input conditions, shown in Figure 1d. For forward power flow operation (battery charge), the constant current control (I_o = 7.8 A) is selected to charge the battery (or load) from V_o = 40 V to 52 V. When the battery voltage reaches 52 V, then the constant voltage control (V_o = 52 V) is selected to charge battery. Figure 8a gives the measured load current, load voltage, and input voltage under V_{in} = 60 V and the forward power flow operation. When V_o is increased from 40 V and $V_o \leq$ 52 V, the load current I_o is controlled at 7.8 A. If the load voltage is reached at 52 V, then the load voltage V_o is controlled at 52 V and the load current is redecreased from 7.8 A. Therefore, the maximum load power is at V_o = 52 V and I_o = 7.8 A. Figure 8b–e show the measured results of the converter under V_{in} = 60 V, I_o = 7.8 A, and V_o = 40 V conditions. The gate signals of S_1–S_4 are provided in Figure 8b. The switching frequency is about 55 kHz. The measured voltage and current of switch S_1 are provided in Figure 8c. It is clear that S_1 is turned on at zero-voltage switching. The experimental waveforms on the primary-side of the converter are given in Figure 8d. The leg voltage $v_{ab} = \pm V_{in} = \pm$60 V. Figure 8e shows the measured results of the resonant current and voltage on the secondary-side of the converter. When $i_{Lr,2}$ is positive (or negative), the voltage $v_{Cr,2}$ is increased (or negative). If $i_{Lr,2}$ = 0, then $v_{Cr,2}$ is kept at a constant value. Similarly, the measured results of the converter under V_{in} = 60 V, I_o = 7.8 A, and V_o = 52 V (maximum power) conditions are given in Figure 8f–i.

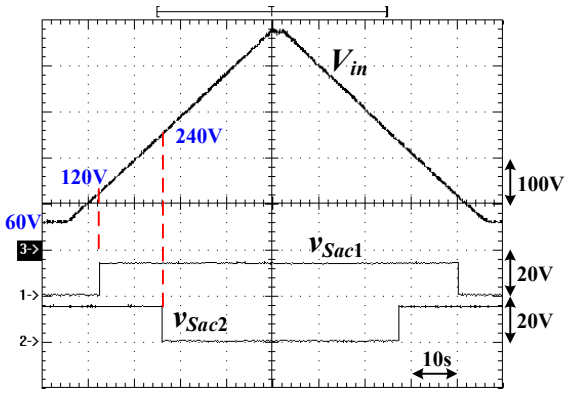


Figure 7. Measured waveforms of V_{in}, S_{ac1}, and S_{ac2}.

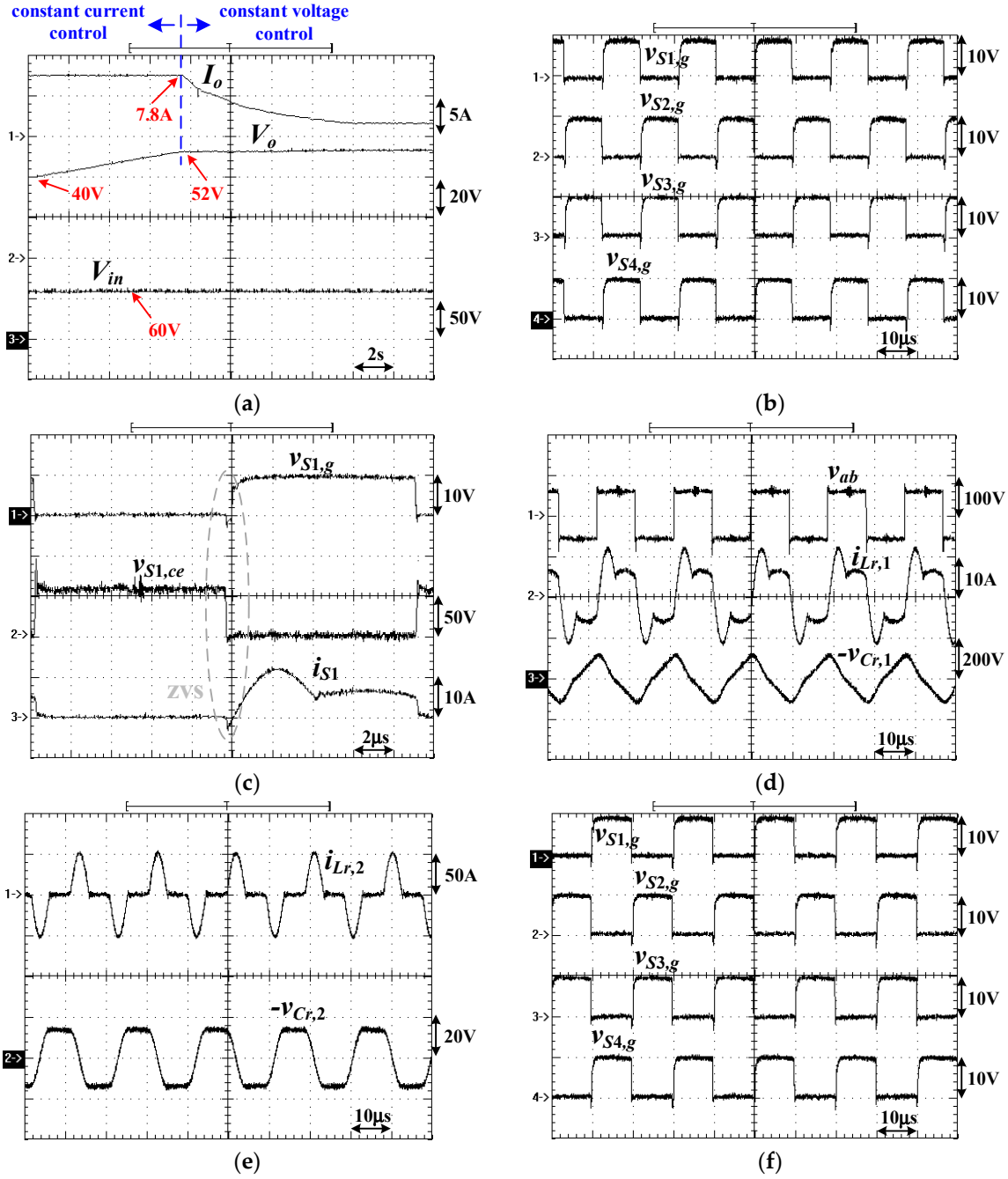


Figure 8. *Cont.*

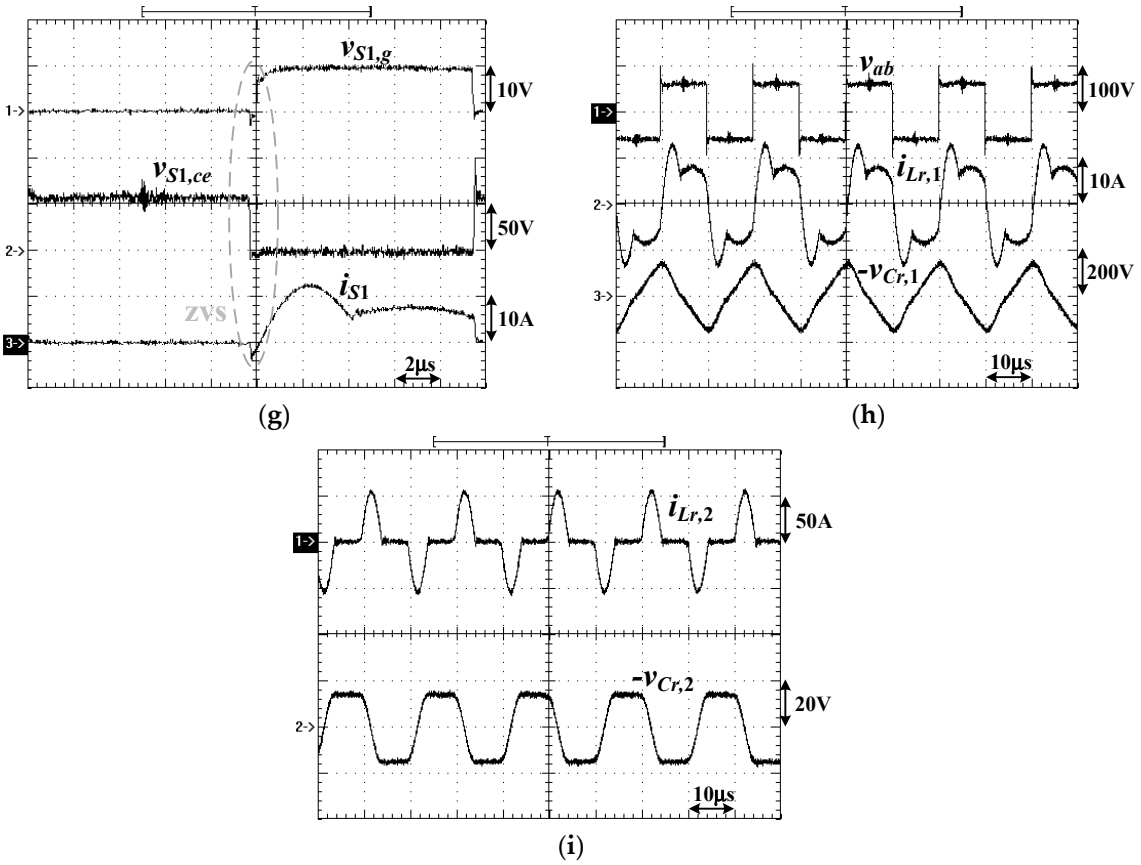


Figure 8. Measured results of the proposed converter under V_{in} = 60 V: (**a**) load current, load voltage, and input voltage under a constant current or constant voltage control; (**b**) the gate voltages of S_1–S_4 under V_o = 40 V; (**c**) $v_{S1,g}$, $v_{S1,ce}$, and i_{S1} under V_o = 40 V; (**d**) v_{ab}, $i_{Lr,1}$, and $-v_{Cr,1}$ under V_o = 40 V; (**e**) $i_{Lr,2}$ and $-v_{Cr,2}$ under V_o = 40 V; (**f**) the gate voltages of S_1–S_4 under V_o = 52 V; (**g**) $v_{S1,g}$, $v_{S1,ce}$, and i_{S1} under V_o = 52 V; (**h**) v_{ab}, $i_{Lr,1}$; and $-v_{Cr,1}$ under V_o = 52 V; (**i**) $i_{Lr,2}$ and $-v_{Cr,2}$ under V_o = 52 V.

The measured results of the converter operated at V_{in} = 118 V and the maximum power (I_o = 7.8 A and V_o = 52 V) condition are provided in Figure 9. From Figures 8 and 9, one can observe that the converter has less voltage gain at V_{in} = 118 V so that the switching frequency of the converter at the V_{in} = 118 V condition is higher than the switching frequency at the V_{in} = 60 V condition. According to Figure 8c,g and Figure 9b, power switch S_1 is turned on at zero-voltage switching for both the V_{in} = 60 V and 118 V cases.

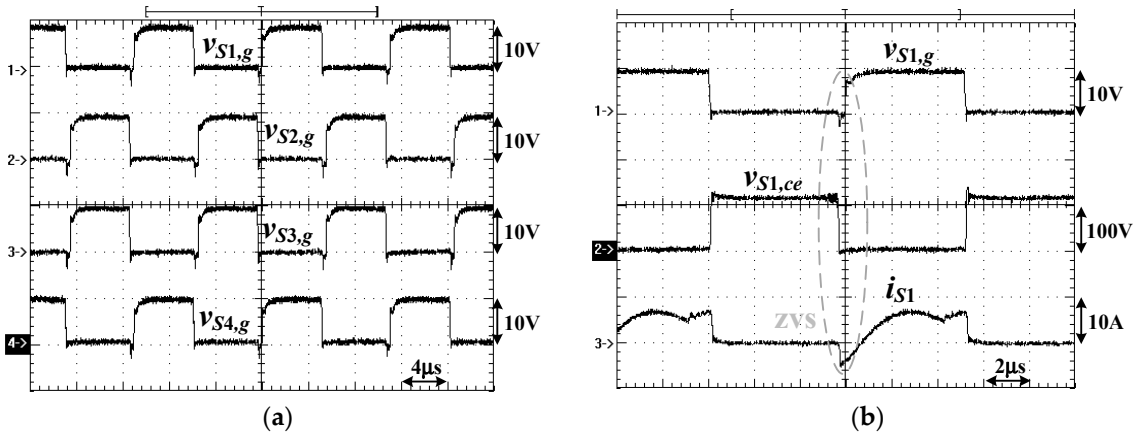


Figure 9. *Cont.*

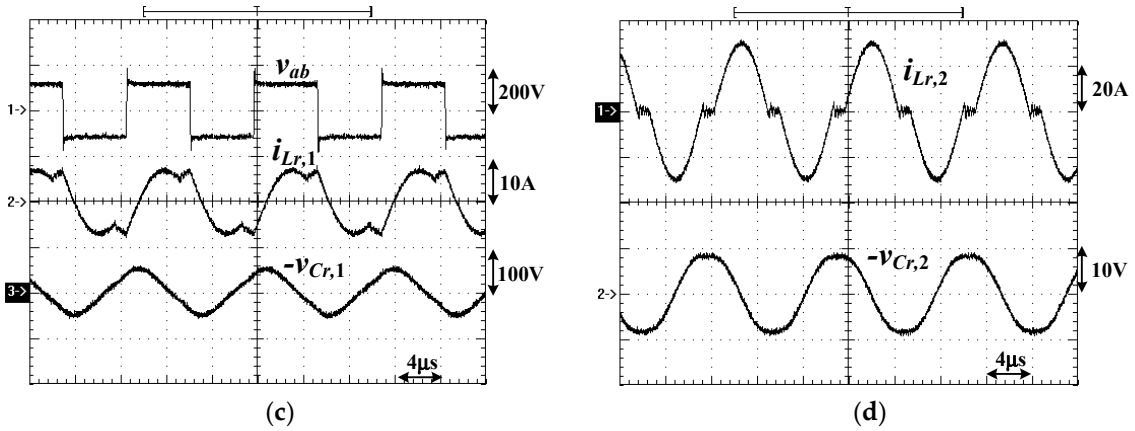


Figure 9. Measured results of the proposed converter under V_{in} = 118 V, V_o = 52 V, and I_o = 7.8 A: (**a**) the gate voltages of S_1–S_4; (**b**) $v_{S1,g}$, $v_{S1,ce}$, and i_{S1}; (**c**) v_{ab}, $i_{Lr,1}$, and $-v_{Cr,1}$; (**d**) $i_{Lr,2}$ and $-v_{Cr,2}$.

Figure 10 gives the test results of the converter under V_{in} = 238 V and the maximum power conditions. The half-bridge resonant circuit and half-wave diode rectifier are used in the converter (Figure 1c) under V_{in} = 238 V input. Only switches S_1 and S_2 are controlled on the left-hand side. Figure 10a gives the gate voltages and resonant current and voltage on the input side. The resonant current and voltage on the output side are provided in Figure 10b. The switch voltage and current of S_1 are provided in Figure 10c. The switching frequency of the converter at V_{in} = 238 V input and full power condition is about 96 kHz, which is close to the resonant frequency (100 kHz). The resonant currents $i_{Lr,1}$ and $i_{Lr,2}$ are quasi-sinusoidal waveforms. Power switch S_1 is also turned on at zero-voltage switching under the V_{in} = 238 V condition (Figure 10c).

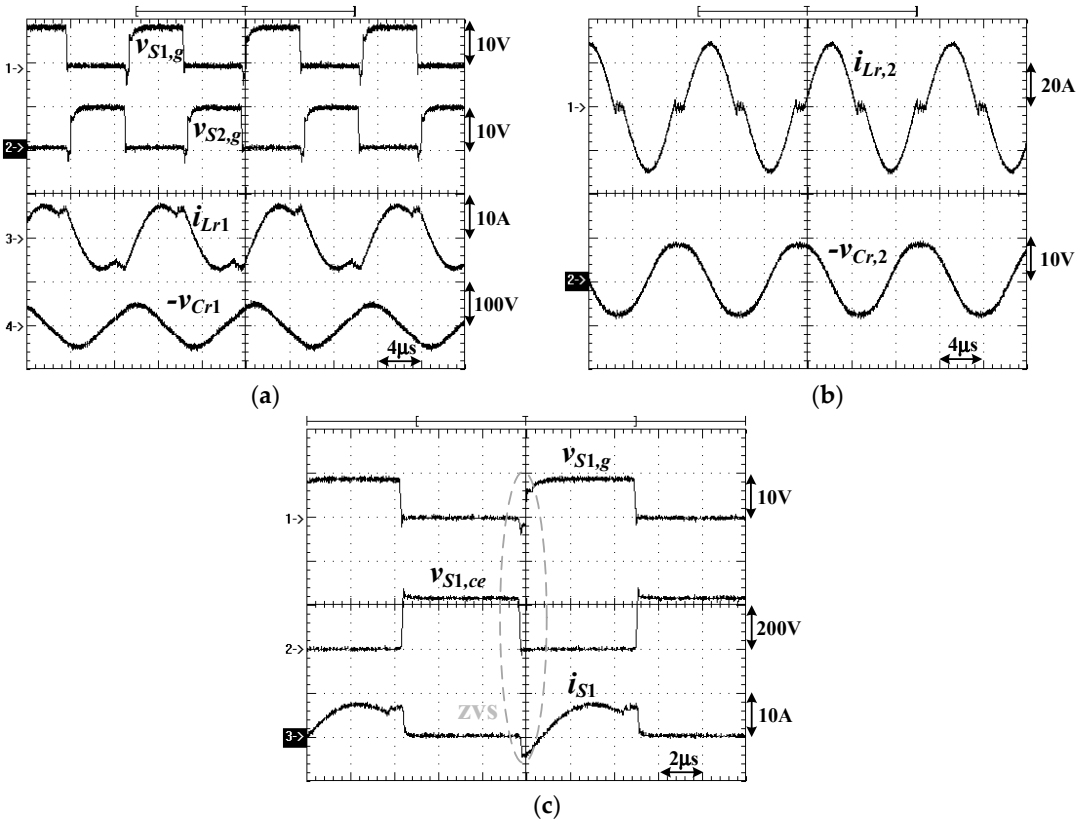


Figure 10. Measured results of the proposed converter under V_{in} = 238 V, V_o = 52 V, and I_o = 7.8 A: (**a**) $v_{S1,g}$, $v_{S2,g}$, $i_{Lr,1}$, and $-v_{Cr,1}$; (**b**) $i_{Lr,2}$ and $-v_{Cr,2}$; (**c**) $v_{S1,g}$, $v_{S1,ce}$, and i_{S1}.

Figure 11 provides the experimental waveforms under V_{in} = 480 V and the maximum power conditions. The half-bridge resonant circuit and full-wave diode rectifier are used on the left-hanf side and right-hand side of the converter (Figure 1d) under the V_{in} = 480 V input. The waveforms $v_{S1,g}$, $v_{S2,g}$, $i_{Lr,1}$, and $-v_{Cr,1}$ are given in Figure 11a. The waveforms $i_{Lr,2}$ and $-v_{Cr,2}$ are provided in Figure 11b. The waveforms $v_{S1,g}$, $v_{S1,ce}$, and i_{S1} are shown in Figure 11c. The switching frequency of the converter at the V_{in} = 480 V input and maximum power condition is about 114 kHz. From the test results in Figure 11c, S_1 is also turned on at zero-voltage switching under V_{in} = 480 V. For the backward power flow operation (from V_o to V_{in}), V_o = 52 V and V_{in} is controlled at 400 V. Therefore, S_5–S_8 are controlled on the right-hand side and the half-wave diode rectifier is operated on the left-hand side (Figure 1e). Figure 12 provides the experimental results under the backward power flow condition. Figure 12a shows the experimental waveforms $v_{S5,g}$–$v_{S8,g}$ and the resonant currents and voltages are provided in Figure 12b. Figure 12c gives the test results of the switch current and voltage of S_5. From the test results in Figure 12, the proposed converter can achieve reverse power flow operation well and switch S_5 on the right-hand side can turn on at zero-voltage switching. The measured circuit efficiencies of the converter are 87.1%, 90.3%, 92.8%, and 93.6% at the V_{in} = 60 V, 118 V, 238 V, and 480 V inputs and maximum power conditions.

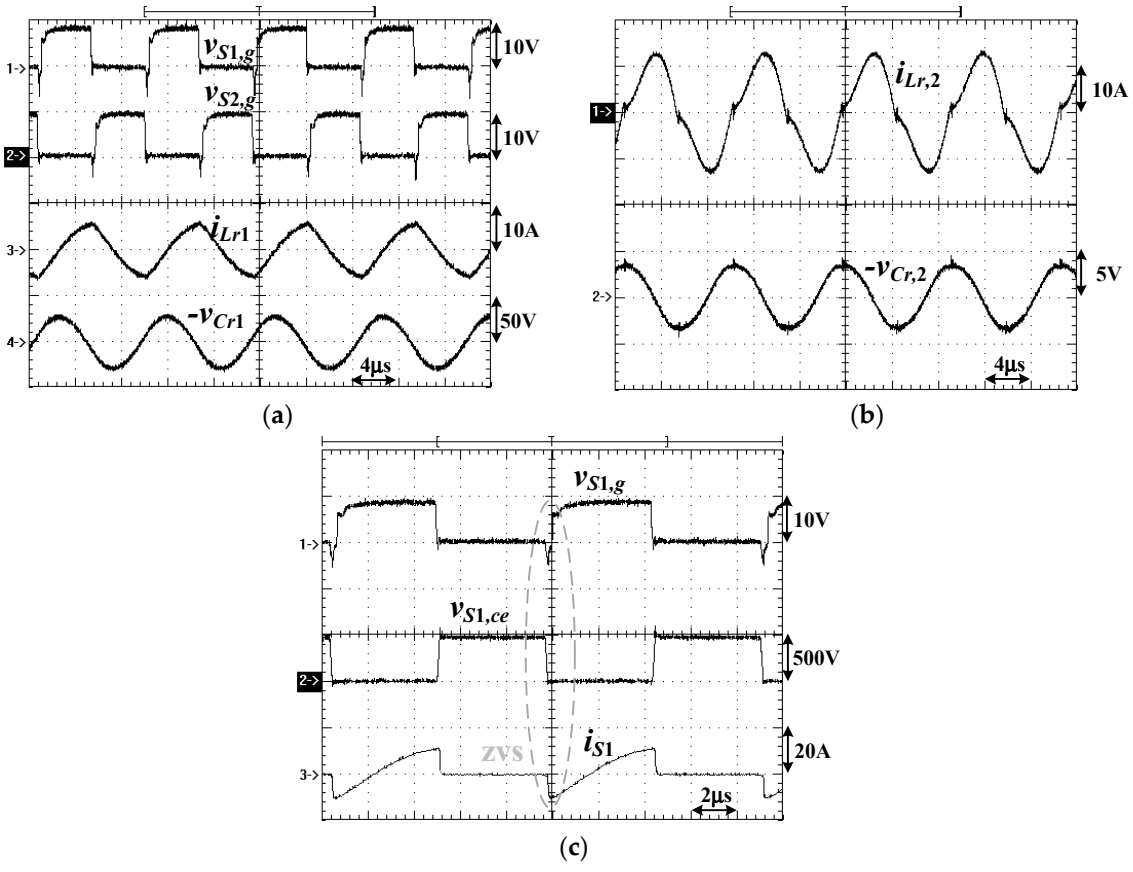


Figure 11. Measured results of the proposed converter under V_{in} = 480 V, V_o = 52 V, and I_o = 7.8 A: (**a**) $v_{S1,g}$, $v_{S2,g}$, $i_{Lr,1}$, and $-v_{Cr,1}$; (**b**) $i_{Lr,2}$ and $-v_{Cr,2}$; (**c**) $v_{S1,g}$, $v_{S1,ce}$, and i_{S1}.

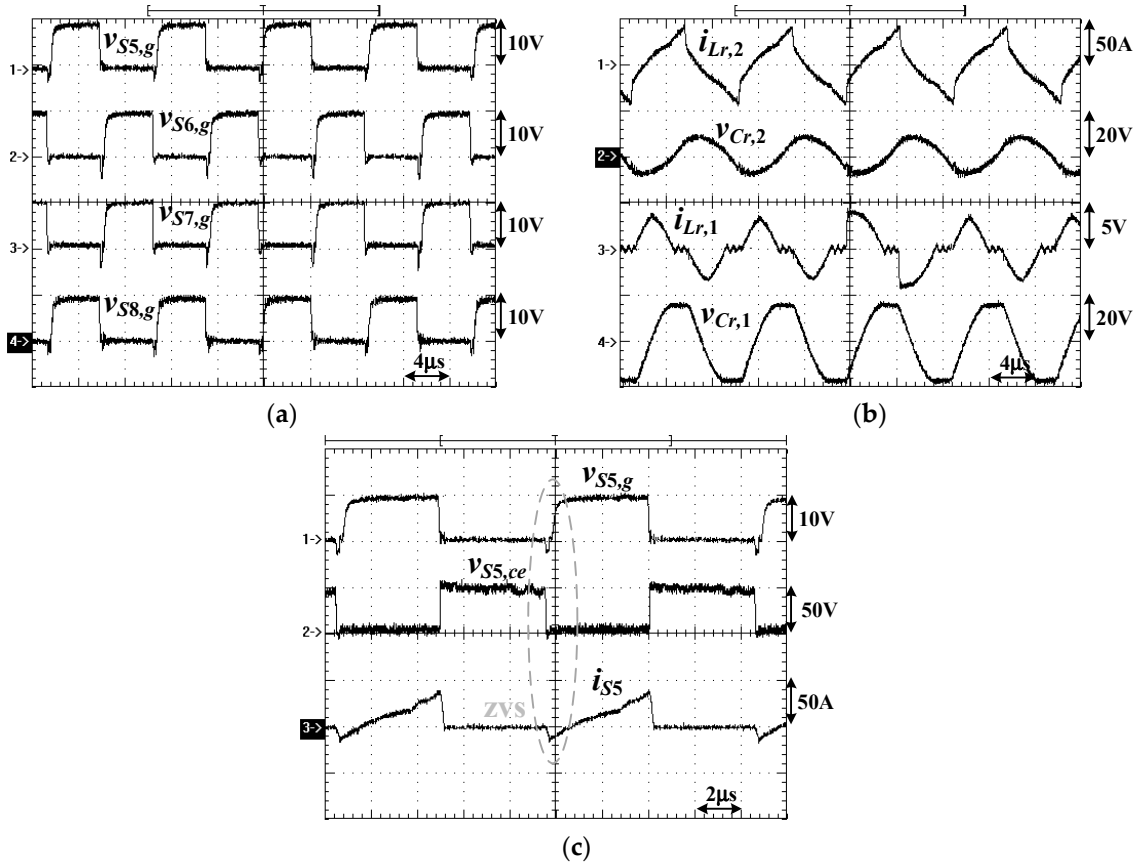


Figure 12. Measured results of the proposed converter under backward power flow operation with V_o = 52 V and V_{in} = 400 V A: (**a**) $v_{S5,g}$–$v_{S8,g}$; (**b**) $i_{Lr,2}$, $v_{Cr,2}$, $i_{Lr,1}$, and $v_{Cr,1}$; (**c**) $v_{S5,g}$, $v_{S5,ce}$, and i_{S5}.

6. Conclusions

In this paper, a hybrid resonant converter is presented and implemented to have wide voltage operation and forward/backward power flow operation for photovoltaic power or battery base applications. The symmetric resonant circuits with a half/full-bridge circuit structure are used on the primary and secondary side to achieve wide voltage operation, such as wide voltage variation on photovoltaic solar panel applications. By selecting the different circuit structures, such as half/full-bridge circuits, the converter can achieve different voltage gain under the input voltage condition. Thus, the drawback of conventional bidirectional resonant converters, such as a narrow voltage range operation, can be improved in the proposed converter. Owing to the resonant circuits on both the primary and secondary sides having the same resonant frequency, the bidirectional power flow can be easily implemented by using a pulse frequency modulation approach. In this paper, the basic circuit structure is presented and discussed in detail. The circuit operation and characteristics are also analyzed and provided. The circuit components of the laboratory prototype were designed, and the experiments are provided to show the benefits of the proposed converter.

Author Contributions: Data curation, Y.-Y.Z.; Formal analysis, B.-R.L.; Investigation, B.-R.L.; Methodology, B.-R.L.; Project administration, B.-R.L.; Validation, B.-R.L.; Writing—original draft, B.-R.L.; Writing—review & editing, B.-R.L. All authors have read and agreed to the published version of the manuscript.

Funding: This research is supported by the National Yunlin University of Science and Technology, Taiwan, under grant number 109H500311.

Acknowledgments: The authors thank the National Yunlin University of Science and Technology, Taiwan, for financial support under grant number 109H500311.

Conflicts of Interest: The authors declare no conflict of interest.

References

1. Emadi, A.; Lee, Y.J.; Rajashekara, K. Power electronics and motor drives in electric, hybrid electric, and plug-in hybrid electric vehicles. *IEEE Trans. Ind. Electron.* **2008**, *55*, 2237–2245. [CrossRef]
2. Dragicevic, T.; Lu, X.; Vasquez, J.C.; Guerrero, J.M. DC microgrids—Part I: A review of control strategies and stabilization techniques. *IEEE Trans. Ind. Electron.* **2016**, *31*, 4876–4891. [CrossRef]
3. Dragicevic, T.; Lu, X.; Vasquez, J.C.; Guerrero, J.M. DC microgrids—Part II: A review of power architectures, applications, and standardization issue. *IEEE Trans. Ind. Electron.* **2016**, *31*, 3528–3549. [CrossRef]
4. Guerrero, J.M.; Loh, P.C.; Lee, T.L.; Chandorkar, M. Advanced control architectures for intelligent microgrids—part II: Power quality, energy storage, and ac/dc microgrids. *IEEE Trans. Ind. Electron.* **2013**, *60*, 1263–1270. [CrossRef]
5. Meng, L.; Shafiee, Q.; Trecate, G.F.; Karimi, H.; Fulwani, D.; Lu, X.; Guerrero, J.M. Review on control of DC microgrids and multiple microgrid clusters. *IEEE J. Emerg. Sel. Top. Power Electron.* **2017**, *5*, 928–948.
6. Mangu, B.; Akshatha, S.; Suryanarayana, D.; Fernandes, B.G. Grid-connected PV-wind-battery-based multi-input transformer-couple bidirectional dc-dc converter for household applications. *IEEE J. Emerg. Sel. Top. Power Electron.* **2016**, *4*, 1086–1095. [CrossRef]
7. Yilmaz, M.; Krein, P.T. Review of battery charger topologies, charging power levels, and infrastructure for plug-in electric and hybrid vehicles. *IEEE Trans. Ind. Electron.* **2013**, *28*, 2151–2169. [CrossRef]
8. Ahrabi, R.R.; Ardi, H.; Elmi, M.; Ajami, A. A novel step-up multi input dc-dc converter for hybrid electric vehicles application. *IEEE Trans. Ind. Electron.* **2017**, *32*, 3549–3561.
9. Tao, H.; Kotsopoulos, A.; Duarte, J.L.; Hendrix, M.A.M. Family of multiport bidirectional DC-DC converters. *IEE Proc. Electr. Power Appl.* **2006**, *153*, 451–458. [CrossRef]
10. Xu, D.; Zhao, C.; Fan, H. A PWM plus phase-shift control bidirectional DC-DC converter. *IEEE Trans. Ind. Electron.* **2004**, *19*, 666–675. [CrossRef]
11. Jain, A.K.; Ayyanar, R. PWM control of dual active bridge: Comprehensive analysis and experimental verification. *IEEE Trans. Ind. Electron.* **2011**, *26*, 1215–1227. [CrossRef]
12. Zhao, B.; Song, Q.; Liu, W.; Sun, Y. Overview of dual-active-bridge isolated bidirectional DC–DC converter for high-frequency-link power-conversion system. *IEEE Trans. Ind. Electron.* **2014**, *29*, 4091–4106. [CrossRef]
13. Rico, S.J.; Pagano, D.J.; Lucas, K.E. Bidirectional power sharing for DC microgrid enabled by dual active bridge DC-DC converter. *Energies* **2021**, *14*, 404.
14. Lara, J.; Masisi, L.; Hernandez, C.; Arjona, A.; Chandra, A. Novel five-level ANPC bidirectional converter for power quality enhancement during G2V/V2G operation of cascaded EV charger. *Energies* **2021**, *14*, 2650. [CrossRef]
15. Jung, J.H.; Kim, H.S.; Ryu, M.H.; Baek, J.W. Design methodology of bidirectional CLLC resonant converter for high-frequency isolation of DC distribution systems. *IEEE Trans. Ind. Electron.* **2013**, *28*, 1741–1755. [CrossRef]
16. Zou, S.; Lu, J.; Mallik, A.; Khaligh, A. Bi-directional CLLC converter with synchronous rectification for plug-in electric vehicles. *IEEE Trans. Ind. Appl.* **2018**, *54*, 998–1005. [CrossRef]
17. Shang, C.; Liu, L.; Liu, M.; Men, S. A highly-efficient two-stage DC-DC converter with wide input voltage. In Proceedings of the 2015 IEEE International Telecommunications Energy Conference, Osaka, Japan, 18–22 October 2015; pp. 1–6.
18. Jeong, Y.; Kim, J.K.; Lee, J.B.; Moon, G.W. An asymmetric half-bridge resonant converter having a reduced conduction loss for DC/DC power applications with a wide range of low input voltage. *IEEE Trans. Power Electron.* **2017**, *32*, 7795–7804. [CrossRef]
19. Lin, B.B.; Chen, K.Y. Hybrid LLC Converter with Wide Range of Zero-Voltage Switching and Wide Input Voltage Operation. *Appl. Sci.* **2020**, *10*, 8250. [CrossRef]
20. Wang, P.; Zhou, L.; Zhang, Y.; Li, J.; Sumner, M. Input-parallel output-series DC-DC boost converter with a wide input voltage range, for fuel cell vehicles. *IEEE Trans. Veh. Technol.* **2017**, *66*, 7771–7781. [CrossRef]
21. Hu, H.; Fang, X.; Chen, F.; Shen, Z.J.; Batarseh, I. A modified high-efficiency LLC converter with two transformers for wide input-voltage range applications. *IEEE Trans. Power Electron.* **2013**, *28*, 1946–1960. [CrossRef]
22. Lin, B.R.; Dai, C.X. Wide Voltage Resonant Converter Using a Variable Winding Turns Ratio. *Electronics* **2020**, *9*, 370. [CrossRef]
23. Steigerwald, R.L. A comparison of half-bridge resonant converter topologies. *IEEE Trans. Power Electron.* **1988**, *3*, 174–182. [CrossRef]